

A band structure scenario for the giant spin-orbit splitting observed at the Bi/Si(111) interface

Emmanouil Frantzeskakis,¹ Stéphane Pons,^{1,2} and Marco Grioni¹

¹Laboratoire de Spectroscopie Electronique, Institut de Physique de la Matière Condensée (ICMP),
Ecole Polytechnique Fédérale de Lausanne (EPFL), station 3, CH-1015 Lausanne, Switzerland

²Département Physique de la Matière et des Matériaux, Institut Jean Lamour,
CNRS, Nancy Université, F-54506 Vandœuvre-les-Nancy, France

(Dated: May 13, 2022)

The Bi/Si(111) ($\sqrt{3} \times \sqrt{3}$)R30° trimer phase offers a prime example of a giant spin-orbit splitting of the electronic states at the interface with a semiconducting substrate. We have performed a detailed angle-resolved photoemission (ARPES) study to clarify the complex topology of the hybrid interface bands. The analysis of the ARPES data, guided by a model tight-binding calculation, reveals a previously unexplored mechanism at the origin of the giant spin-orbit splitting, which relies primarily on the underlying band structure. We anticipate that other similar interfaces characterized by trimer structures could also exhibit a large effect.

I. INTRODUCTION

The normal spin degeneracy of the electronic states of non-magnetic solids is lifted by the spin-orbit (SO) interaction in crystals lacking an inversion center (Dresselhaus effect) [1, 2]. A similar effect was predicted theoretically by Rashba and Bychkov (RB) for a two-dimensional electron gas (2DEG) at a surface or an interface which exhibits a structural surface asymmetry (SSA) [3]. Although the model was originally motivated by semiconductor heterojunctions, the first direct observation of split bands by angle-resolved photoemission spectroscopy (ARPES) was made on metal surfaces [4–10]. Like its atomic counterpart, the RB effect has a relativistic origin, namely the coupling of the spin to the magnetic field which appears in the rest frame of the electron. In the free-electron limit considered by RB, the parabolic dispersion is split, as in Fig. 1, into two branches of opposite spin:

$$E^{\pm}(k) = \frac{\hbar^2 k^2}{2m^*} \pm \alpha_R k, \quad (1)$$

where k is the magnitude of the electron momentum in the plane of the surface, and m^* the (effective) mass. The Rashba parameter α_R is proportional to the gradient of the surface electric potential, and defines the strength of the RB effect. The SO-splitting of the two branches can be quantified by their momentum offset $2k_0 = 2\alpha_R m^* / \hbar^2$ or, equivalently, by the Rashba energy $E_R = \hbar^2 k_0^2 / (2m^*)$, the difference between the band minimum ($m^* > 0$) or maximum ($m^* < 0$) and the crossing point of the two branches at $k = 0$. In a more realistic approach, the band splitting depends not only on the surface potential gradient, but also on the atomic SO parameter, and on the asymmetry of the electron wavefunctions [10–13].

Interest in the RB effect has been revamped by observations of a *giant* SO-splitting in surface alloys formed by a high-Z element – Bi or Pb – at the Ag(111) surface [14]. The unusual strength of the effect has prompted a reassessment of the various factors contributing to the effect. It has been suggested that additional components of the surface potential gradient *within* the surface, reflecting the anisotropic charge distribution, are probably important [15]. Independent studies

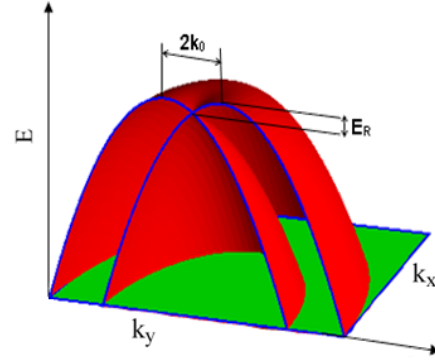


FIG. 1: (color online) Schematics of the RB SO split bands for a 2D free electron gas

have stressed structural aspects, namely the role of relaxation and buckling of the topmost layer in defining the hybrid states [16].

Metallic surface alloys with a giant SO splitting are potentially interesting for spintronics applications. The present challenge is to make them compatible with semiconductor technology [17, 18]. There has been encouraging progress in this direction, and several attempts have been made to grow thin buffer layers supporting SO-split bands at their surface on Si(111) substrates [19–21]. Recently, a giant spin-splitting with no buffer layers was demonstrated for the isostructural Bi/Si(111) [22, 23] and Bi/Ge(111) [24] interfaces. In the same line, metallic spin-split surface states were observed in the related Pb/Ge(111) system [25]. In all cases, the electronic structure of these interfaces is more complex than that predicted by the simple RB model. Although first-principles calculations reproduce the experimental results, they suffer from a certain lack of transparency. This leaves room for a simpler but more direct approach which can help in the interpretation of the experimental data, and thus contribute to clarify the unconventional properties of the electronic states. This was the motivation of the present work, which compares the results of a detailed experimental band mapping of the Bi/Si(111) interface by ARPES, with simple models of the band structure in the presence of a RB-like interaction. In particular, a para-

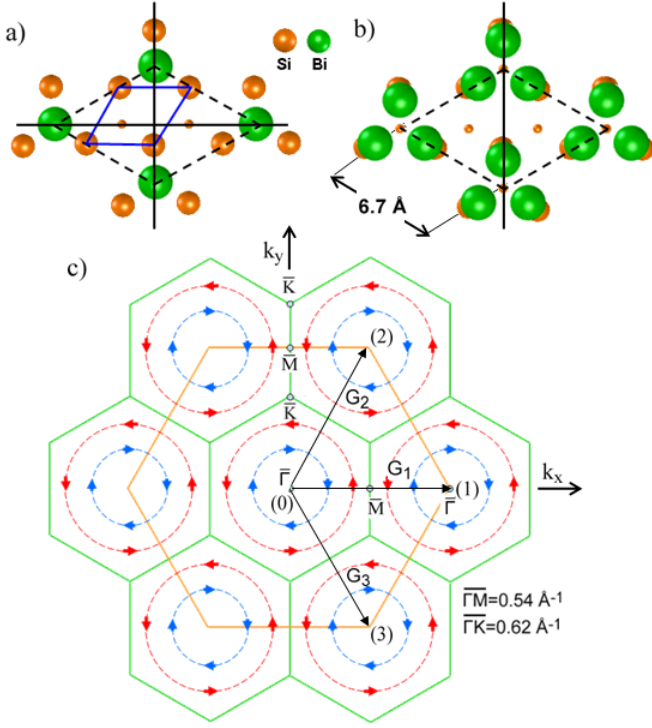


FIG. 2: (color online) The structure of (a) the monomer (α -) and (b) the trimer ($\beta - \sqrt{3} \times \sqrt{3}$)R30° Bi/Si(111) phases. The size of the Si atoms indicates their distance from the surface. Solid (dashed) lines indicate the 1×1 ($\sqrt{3} \times \sqrt{3}$) primitive unit cell. The horizontal and vertical black lines follow the mirror planes of the overlayers. (c) The 1×1 (large hexagon) and ($\sqrt{3} \times \sqrt{3}$)R30° (small hexagons) SBZs. The circles are constant-energy contours for RB paraboloids centered at each equivalent $\bar{\Gamma}$ point of the latter, and the arrows indicate the spin polarization. The reciprocal lattice vectors \mathbf{G}_1 , \mathbf{G}_2 and $\mathbf{G}_3 = \mathbf{G}_1 - \mathbf{G}_2$ are those considered in the NFE model of Sections III (B) and (C)

metric tight-binding scheme provides a satisfactory qualitative description of the data, and suggests a possible new mechanism to achieve a large spin polarization, which is closely connected with a characteristic feature of the band structure of the interface.

II. EXPERIMENTAL DETAILS

The Si(111) substrate (Sb-doped, resistivity $0.01\Omega\cdot\text{cm}$) was flashed at 1200°C by direct current injection, and then cooled slowly in order to obtain a sharp low-energy electron diffraction (LEED) (7×7) pattern. The ($\sqrt{3} \times \sqrt{3}$)R30° Bi/Si(111) interface was prepared by deposition of 1 monolayer (ML) of Bi from a calibrated EFM3 Omicron source on the the substrate at RT followed by a mild annealing. ARPES spectra were acquired at 70 K and 21.2 eV photon energy, with a PHOIBOS 150 SPECS Analyzer equipped with a monochromatized GammaData VUV 5000 high brightness source. The Fermi level position was determined from the Fermi edge of a

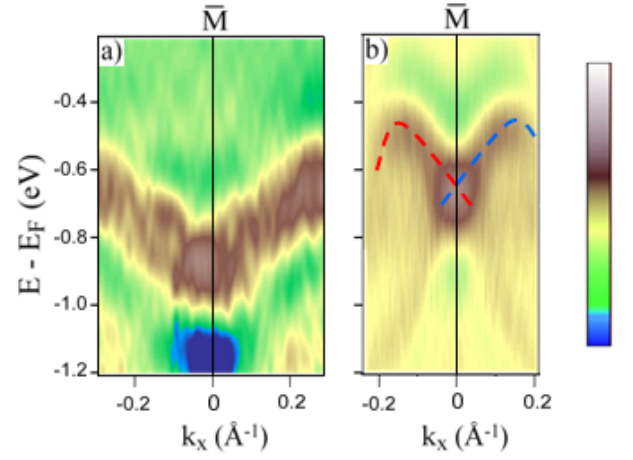


FIG. 3: (color online): 2nd derivative ARPES intensity map along the $\bar{\Gamma}\bar{M}$ direction for the monomer (a) and the trimer (b) phases of Bi/Si(111).

polycrystalline Au sample.

III. RESULTS AND MODEL CALCULATIONS

A. ARPES Measurements

The Bi/Si(111) interface exhibits two different structures with the same ($\sqrt{3} \times \sqrt{3}$)R30° Bi/Si(111) periodicity: a monomer structure (α -phase) for a coverage of $1/3$ ML, and a trimer structure (β -phase) for 1 ML coverage. They are illustrated in Fig. 2 (a) and (b). According to the widely accepted T₄ model [26], both monomers and trimers are centered above the 2nd layer Si substrate atoms. Figure 2(c) shows the surface Brillouin zones (SBZ) of the unreconstructed Si(111) surface, and of the ($\sqrt{3} \times \sqrt{3}$)R30° superstructure. In the following we will always refer to the latter. The α and β phases have quite different band structures, and can be easily distinguished. This is illustrated in Fig. 3, where (second derivative) ARPES intensity maps of the two phases are compared around the \bar{M} point. In agreement with previous studies, the α -phase shows a rather flat surface state with a broad minimum at \bar{M} [27], while the β -phase shows two symmetrically dispersing features crossing at \bar{M} [28, 29]. In the rest of the paper we only consider the trimer β -phase, which is the most interesting in the present context. The system has a threefold rotation axis, and three mirror planes perpendicular to the surface. One of these mirror planes is parallel to the $[1\bar{1}2]$ direction, and also to the $\bar{\Gamma}\bar{K}\bar{M}$ direction of the SBZ (k_y axis in Fig. 2 (c)). The other mirror planes are rotated by 120° around the z axis. The overlayer symmetry is identical to the one of the substrate and corresponds to the plane group $p31m$. The characteristic band crossing at \bar{M} is the signature of a peculiar RB-type SO-splitting with a momentum offset k_0 of 0.126 \AA^{-1} and a Rashba energy of 140 meV [22, 23]. The large splitting has been previously associ-

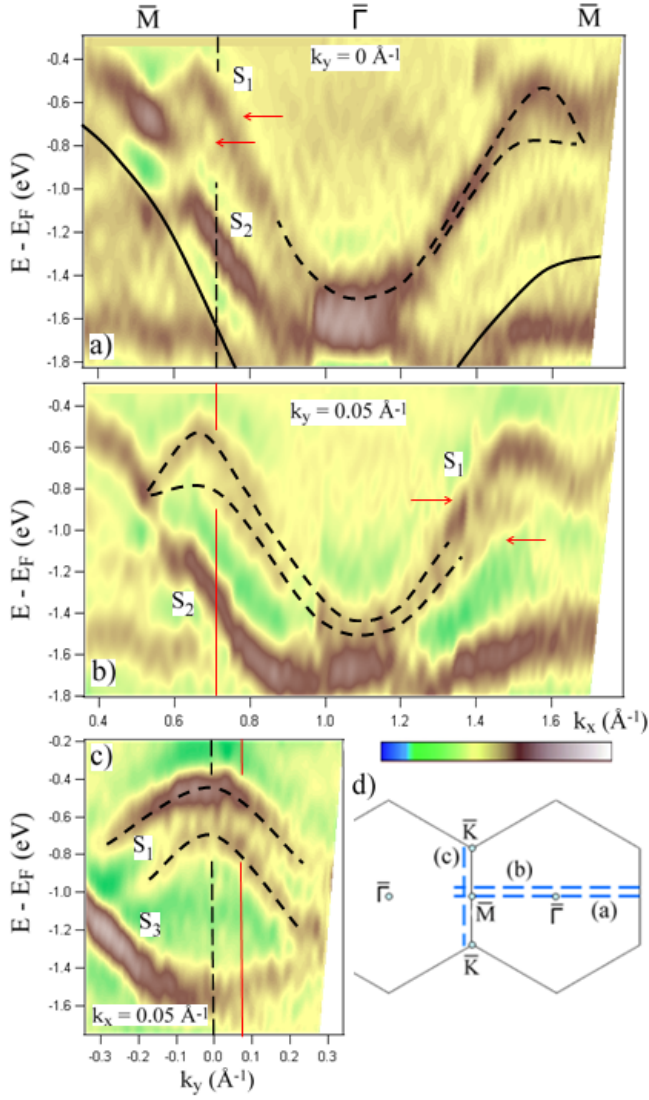


FIG. 4: (color online) (a) to (c) Second-derivative ARPES intensity maps showing the band structure along the k -space cuts (a) to (c) of panel (d). The dashed curves and arrows are guides to the eye which highlight the dispersion of the S_1 split branches. The thick solid line marks the edge of the projected Si bulk gap. Images (a) and (b) intersect image (c) respectively along the vertical dashed and solid lines.

ated with the inversion asymmetry induced by the trimers. We will see later that a different interpretation is possible.

The ARPES intensity maps of Fig. 4 illustrate the dispersion of three surface states – labelled S_1 to S_3 as in Ref. 23 –, along two high-symmetry lines. All three states are predicted to be spin-polarized [23]. S_1 exhibits a large splitting around \bar{M} , as already shown by Fig. 3, and a peculiar anisotropic dispersion around that point. The experimental dispersion along the $\bar{\Gamma}\bar{M}\bar{\Gamma}$ line (Fig. 4 (a)) shows a hint of the two branches predicted by theory [22, 23] and highlighted by dashed lines, which split away from the crossing point at \bar{M} . The two S_1 branches merge again approaching the $\bar{\Gamma}$ point, where they cannot be resolved from S_2 . The energy splitting of the two

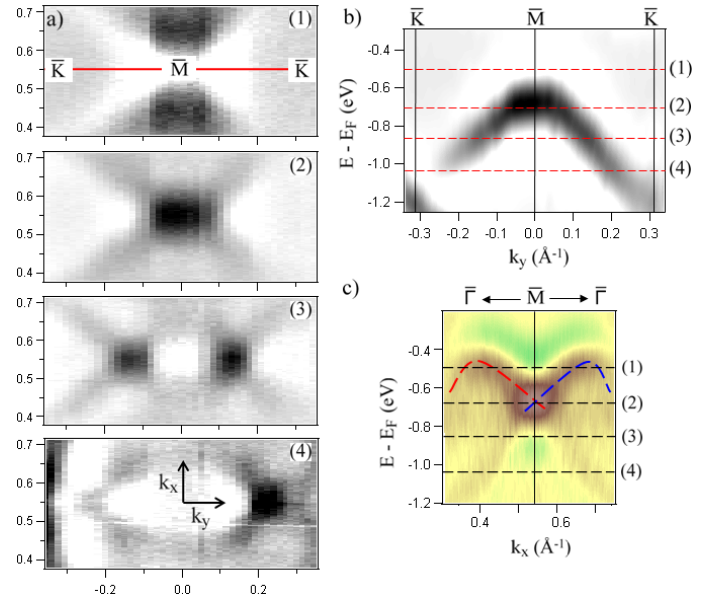


FIG. 5: (color online) (a) Experimental CE maps around \bar{M} . The corresponding binding energies are 0.53, 0.68, 0.84, and 1.02 eV for panels (1) to (4). They are indicated by horizontal dashed lines in the intensity maps of panels (b) and (c), taken along the $\bar{K}\bar{M}\bar{K}$ and $\bar{\Gamma}\bar{M}\bar{\Gamma}$ directions. In the gray-scale plots, highest intensity is black.

branches increases away from the $\bar{\Gamma}\bar{M}\bar{\Gamma}$ high-symmetry line, as shown by Fig. 4 (b) which shows the dispersion along the parallel cut (b) of Fig. 4 (d) (i.e. $k_y \neq 0$). The split branches of S_1 are clearly resolved in Fig. 4 (c) which shows a cut parallel to the $\bar{K}\bar{M}\bar{K}$ line. Along this line the intensity of S_2 is very small due to ARPES matrix elements. The images of Fig. 4 (a) and (b) intersect the perpendicular cut (c) along respectively the vertical black dashed and the red solid lines.

Figure 5 illustrates the unusual topology of surface band S_1 around the \bar{M} point, in a region of k -space where it is well separated from other surface or bulk-derived features. Panels 1 to 4 of Fig. 5 (a) show constant-energy (CE) cuts taken at increasing binding energies between 0.53 and 1.02 eV, corresponding to the horizontal dashed lines in the intensity maps along the $\bar{K}\bar{M}\bar{K}$ and $\bar{\Gamma}\bar{M}\bar{\Gamma}$ directions of panels (b) and (c). Starting at the highest binding energy, the CE maps show two intersections along $\bar{K}\bar{M}\bar{K}$, symmetrically located with respect to \bar{M} . They get closer at lower binding energy, following the negative-mass dispersion of Fig. 5 (b). The two intersections finally merge at \bar{M} for $E_B \sim 0.68$ eV. This is the maximum of the dispersion along $\bar{K}\bar{M}\bar{K}$, and the crossing point of the two SO-split branches along the perpendicular $\bar{\Gamma}\bar{M}\bar{\Gamma}$ direction. Panel 1, taken above this energy, indeed shows non-intersecting CE contours.

The data of Fig. 5 reveals that the topology of S_1 is quite different from that of Fig. 1, predicted by the usual Rashba model for a free-electron band centered at the $\bar{\Gamma}$ point. The degeneracy of the SO-split branches at \bar{M} is required by a combination of time-reversal and translational symmetry. On the other hand, the line of (near) spin degeneracy of Fig. 5 (b)

finds no correspondence in the simple Rashba model. The experimentally observed large difference of the energy splitting along the two high-symmetry directions is well captured by first-principles calculations [22, 23].

B. An Isotropic Nearly-Free Electron Model

We will now attempt a comparison of the experimental data using simple theoretical models, to gain further insight in the unusual dispersion of the SO-split bands. The minimal requirement for any model is that it should include both the Rashba-like interaction and translational invariance. The simplest approach satisfying this condition is an isotropic nearly-free electron (NFE) model. This model is schematically illustrated in Fig. 2 (c). RB paraboloids ($m^* > 0$) are centered at all equivalent $\bar{\Gamma}$ points, and the CE lines are concentric circles representing the inner and outer SO-split branches. The spins exhibit a vortical structure around the $\bar{\Gamma}$ points. Two paraboloids centered at two adjacent SBZ intersect in the common $\overline{\text{KMK}}$ Bragg plane along two parabolas, one at lower energy for the outer SO branch, and a second at higher energy for the inner.

The Rashba hamiltonian for a free-electron is [3]:

$$H_{\text{RB}}(\mathbf{k}) = \alpha_R(\boldsymbol{\sigma} \times \mathbf{k})_z, \quad (2)$$

where $\boldsymbol{\sigma}$ is the vector of Pauli matrices. In a representation where the basis states are $|\mathbf{k} \uparrow\rangle$, $|\mathbf{k} \downarrow\rangle$, and spin projections refer to the z axis, the corresponding matrix is:

$$H_{\text{RB}}(\mathbf{k}) = \begin{pmatrix} \hbar^2 k^2 / 2m & \alpha_R(k_y + ik_x) \\ \alpha_R(k_y - ik_x) & \hbar^2 k^2 / 2m \end{pmatrix}. \quad (3)$$

Diagonalization of this hamiltonian generates SO-split paraboloids centered at $\bar{\Gamma}$ as in Fig. 1. The corresponding ‘spin-up’ and ‘spin-down’ eigenstates refer to a quantization axis $\mathbf{e}_\theta = \mathbf{e}_z \times \mathbf{k}/k$, which is always perpendicular to \mathbf{k} , i.e. tangential to the constant-energy circles. These states are therefore 100% in-plane polarized, with a purely tangential spin polarization \mathbf{P} – opposite on the two branches – rotating around $\bar{\Gamma}$. This is easily generalized to include the lattice periodicity. Since we are mainly interested in the band structure near E_F around the $\bar{\text{M}}$ point, it is a good approximation, to consider only the first SBZ and three adjacent zones centered at the lattice vectors $\mathbf{G}_1 = (1, 0)$, $\mathbf{G}_2 = (0, 1)$ and $\mathbf{G}_3 = \mathbf{G}_1 - \mathbf{G}_2$, as in Fig. 2 (c). The basis vectors, again referred to the z axis, are $|\mathbf{k} \uparrow\rangle$, $|\mathbf{k} \downarrow\rangle$, $|\mathbf{k} + \mathbf{G}_1 \uparrow\rangle$, $|\mathbf{k} + \mathbf{G}_1 \downarrow\rangle$, $|\mathbf{k} + \mathbf{G}_2 \uparrow\rangle$, $|\mathbf{k} + \mathbf{G}_2 \downarrow\rangle$, $|\mathbf{k} + \mathbf{G}_3 \uparrow\rangle$, $|\mathbf{k} + \mathbf{G}_3 \downarrow\rangle$. The truncated NFE hamiltonian matrix is then:

$$H_{\text{NFE}} = \begin{pmatrix} H_{\text{RB}}(\mathbf{k}) & V_{01} & V_{02} & V_{03} \\ V_{01}^* & H_{\text{RB}}(\mathbf{k} + \mathbf{G}_1) & V_{12} & V_{13} \\ V_{02}^* & V_{12}^* & H_{\text{RB}}(\mathbf{k} + \mathbf{G}_2) & V_{23} \\ V_{03}^* & V_{13}^* & V_{23}^* & H_{\text{RB}}(\mathbf{k} + \mathbf{G}_3) \end{pmatrix}. \quad (4)$$

The diagonal 2×2 building blocks now generate SO-split paraboloids centered at $\bar{\Gamma}$, and at \mathbf{G}_1 , \mathbf{G}_2 and \mathbf{G}_3 . The off-diagonal 2×2 blocks describe the interaction between states of equal spin on the various paraboloids [30]. The hybridization strength is, as usual, the corresponding Fourier component of the crystal potential $V(r)$ defined by:

$$V(r) = \sum_i V_{G_i} e^{i\mathbf{G}_i \cdot \mathbf{r}}. \quad (5)$$

For instance:

$$V_{01} = \begin{pmatrix} V_{G_1} & 0 \\ 0 & V_{G_1} \end{pmatrix}. \quad (6)$$

It is easy to show that (6) is equivalent to an interaction of the form $V(\mathbf{k}, \mathbf{k} + \mathbf{G}_1) = V_{G_1} \cos(\delta/2)$, where δ is the angle between the two polarization vectors. In our case all hybridization terms are equal: $V_{G_i} = V_G$, and H_{NFE} contains only the two parameters α_R and V_G . The binding energy of the

paraboloids at $\bar{\Gamma}$, or equivalently the Fermi level position, are adjusted to fit the experimental data of Fig. 4.

Figure 6 (a) illustrates the predictions of the NFE model along the $\bar{\Gamma}\text{M}\bar{\Gamma}$ direction, in the limit $|V_G| = 0$. The outer branches cross at the $\bar{\text{M}}$ point, with opposite spin polarization. Along the perpendicular $\overline{\text{KMK}}$ direction (Fig. 6 (c)), their intersection is a parabola dispersing upwards from $\bar{\text{M}}$. The inner branches of the paraboloids similarly cross above E_F . The model yields a constant momentum separation between the SO-split branches of each paraboloid, and does not capture the experimentally observed k -dependent splitting. Moreover, the sign of the dispersion along the SBZ boundary is opposite to that of Fig. 5 (b), and the opposite spin states are strictly degenerate, for any value of α_R .

Figure 6 (b) shows that the main effect of a finite lattice potential is the opening of energy gaps at the crossing of bands with parallel spins, i.e. at the crossing of the outer branch of one paraboloid with the inner branch of the paraboloid centered at an adjacent SBZ. No gap opens when either the outer or the inner branches cross at the $\bar{\text{M}}$ point, because their spins

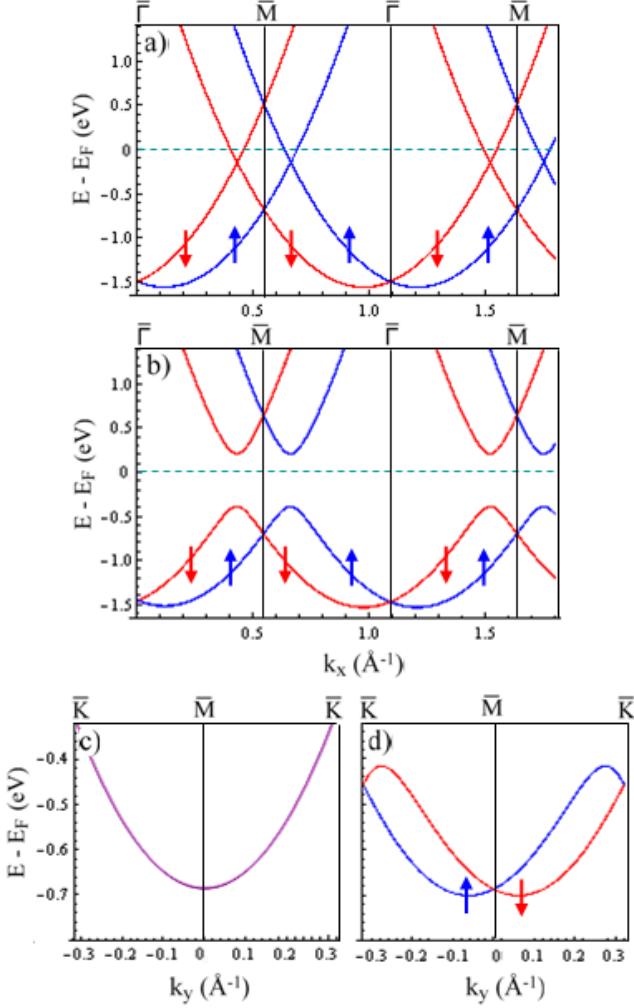


FIG. 6: (color online) (a), (b) Band dispersion of the isotropic NFE model along the $\bar{\Gamma}\bar{M}\bar{\Gamma}$ for $|V_G| = 0$ and $|V_G| = 0.3$ eV. Arrows indicate the opposite (in-plane) spin polarization of the two branches. (c), (d) Same for the $\bar{K}\bar{M}\bar{K}$ high-symmetry direction. The two spin states are degenerate along the SBZ boundary for $|V_G| = 0$. Notice the different scales in (a), (b) and (c), (d).

are opposite there. This is consistent with the requirements of time-reversal symmetry. At the other crossing points along the SBZ boundary the spins are not strictly opposite, but they are nonetheless rather antiparallel, and the hybridization is therefore small. Therefore, as shown in Fig. 6 (d), the two spin states are not degenerate as in the case $|V_G| = 0$, but their energy separation is small along this direction. The model again yields a positive effective mass, in contrast with the experiment. The momentum splitting along $\bar{K}\bar{M}\bar{K}$ scales with $|V_G|$ and $\alpha^{1/2}$, confirming the unconventional character of the underlying mechanism. It should also be noted that although the \bar{M} spin degeneracy is fundamental, the degeneracy predicted \bar{K} is accidental. It is lifted when further reciprocal lattice points are included.

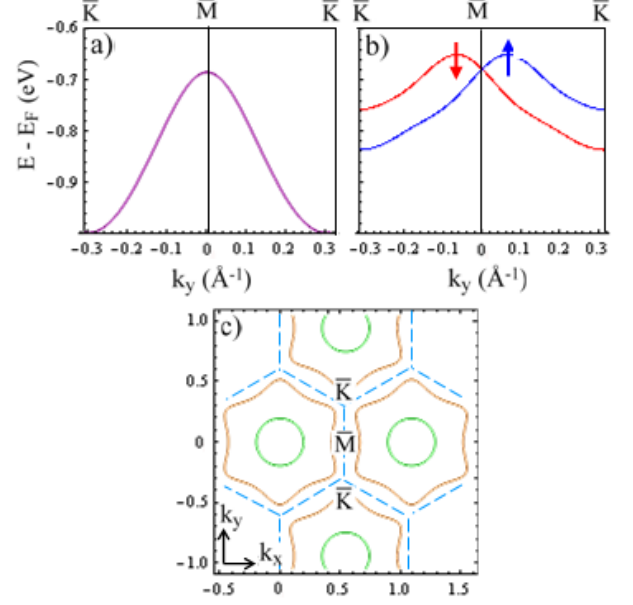


FIG. 7: (color online) (a), (b) Band dispersion of the anisotropic NFE model along the $\bar{K}\bar{M}\bar{K}$ SBZ boundary for $|V_G| = 0$ and $|V_G| = 0.3$ eV. (c) Constant energy contours for a binding energy of 1.1 eV showing the anisotropic shape of the spin-split states. Green (light gray) and brown (dark gray) colors indicate positive and negative values of tangential spin polarization.

C. An Anisotropic Nearly-Free Electron Model

The positive effective mass along the Bragg planes predicted in Fig. 6 (c), (d) is a direct consequence of the simple circular CE contours of the isotropic NFE model. More complex contours are however possible in anisotropic 2D systems. Blossom-like contours have been predicted for Rashba systems [14, 15], and experimentally observed for the BiAg_2 [22] and SbAg_2 [31] surface alloys. Concave CE contours are a generic effect of an in-plane anisotropy of the potential and they are not limited to surface alloys. For example, a 2D Dirac fermion state at the surface of the topological insulator Bi_2Te_3 exhibits a snow-flake-like Fermi surface [32].

In Ref. 32 the author used $\mathbf{k} \cdot \mathbf{p}$ theory to calculate higher-order terms in the effective Hamiltonian of a topological insulator with $R3\bar{m}$ symmetry. Following these results we introduce an anisotropy in $H_{\text{NFE}}(k)$ as:

$$H_{\text{an}}(k) = H_{\text{NFE}}(k) + H'(k), \quad (7)$$

with

$$H'(k) = \frac{c}{2}((k_y + ik_x)^3 + (k_y - ik_x)^3)\sigma_z. \quad (8)$$

This yields:

$$E^\pm(k) = \frac{\hbar^2 k^2}{2m^*} \pm \sqrt{(\alpha_R)^2 k^2 + c^2 k^6 \cos^2(3\theta)}, \quad (9)$$

where c is an anisotropy parameter, and θ is the in-plane angle from the $\bar{\Gamma}\bar{M}$ direction. For small values of c this expression

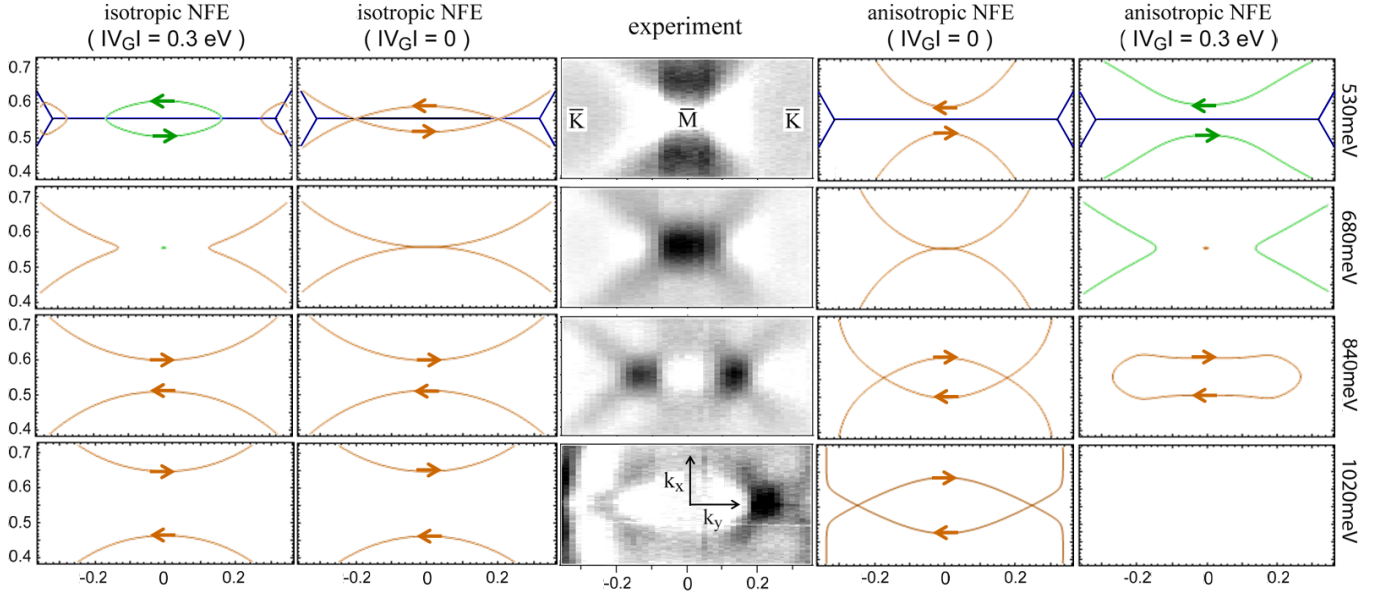


FIG. 8: (color online) Constant energy maps as measured by ARPES (middle panel) and according to the predictions of the isotropic (left panels) and the anisotropic (right panels) NFE models described in the text. Both models are presented for $|V_G| = 0$ and $|V_G| = 0.3$ eV. Green (light gray) and brown (dark gray) colors indicate positive and negative values of tangential spin polarization. The arrows are a sketch of the predicted in-plane projection of the spin polarization around the \bar{M} point.

reduces to the free-electron case with RB splitting (Eq. (1)). The in-plane asymmetry could be self-consistently included starting from Eq. (5), but Eq. (7) provides a minimal alternative model with the single parameter c . The resulting band dispersion agrees well that of the anisotropic 2DEG proposed by Premper et al. [15]. It is shown in Fig. 7 (a) for $|V_G| = 0$, and (b) for $|V_G| = 0.3$ eV. The corresponding parameters are summarized in the Appendix. The model correctly predicts a negative effective mass along $\bar{K}M\bar{K}$. Again, the crystal potential induces a weak RB splitting. The dispersion along $\bar{\Gamma}M\bar{\Gamma}$ is essentially identical to the isotropic case, and is not shown. The CE contours evolve continuously with increasing energy from circular to blossom-like, as in Fig. 7 (c). It should be noted that the spin polarization has only an in-plane tangential component for an isotropic 2DEG, whereas a sizeable out-of-plane and a small radial component are present for the anisotropic case [15]. Figure 8 compares the experimental CE contours around \bar{M} with the predictions of the isotropic (left panels) and the anisotropic (right panels) NFE models. The latter describes reasonably well the data for $|V_G| = 0$, but the agreement is completely spoiled by a finite lattice potential.

A closer examination of the CE contours of reveals another subtler inaccuracy of the anisotropic NFE model. One can identify the mirror plane dictated by the three-dimensional spin polarization vector by comparing the CE contours of Fig. 7 (c) with the predictions of Ref. 15. These authors have computed \mathbf{P} for all k -values on a hexagonal system having a three-fold axis and three equivalent mirror planes. They concluded that the orientation of the 3D spin polarization vector breaks the sixfold symmetry of the underlying contours. In order to find the value of \mathbf{P} one has to perform a numerical computa-

tion of the eigenvectors of Eq. (7) and subsequently calculate the spin expectation values by the operation of the Pauli matrices. This heavy theoretical task is beyond the scope of our model. Nevertheless, by analogy to the conclusions of Ref. 15, one can have a "feeling" about the orientation of \mathbf{P} at different k -points even without knowing its absolute value. As in the case of an isotropic RB model, the two eigenvalues of Eq. (7) indicate opposite values of tangential spin polarization (i.e. red and blue color in Fig. 2 (c)), while by following Premper et al., the small radial component aligns the in-plane projection of the spins with the sixfold contours of the system [15]. According to the same authors, it is the orientation of the finite out-of-plane component which breaks the sixfold symmetry of the underlying contours. In their work this happens by removing the mirror planes which point along the tips of the outer blossom-like contours. These generic results can be applied to our system since it has the same symmetry. The orientation of the Bi trimers leaves $\bar{\Gamma}KM\bar{\Gamma}$ as the only mirror plane. Therefore, by analogy to the conclusions of Ref. 15, one may expect that the symmetry-required orientation of \mathbf{P} would be satisfied only if the outer hexagon tips lie within the $\bar{\Gamma}M\bar{\Gamma}$ rather than the $\bar{\Gamma}KM\bar{\Gamma}$ directions as in Fig. 7 (c). The predicted contours are therefore not consistent with the structural symmetry of our system. This inconsistency is removed by the tight-binding model considered in the following section.

D. An Empirical Tight-Binding Model

The covalent character of the bonds and the semiconducting nature of the Bi-Si(111) interface suggest that local orbitals

may provide a better starting point to describe its electronic properties. We have performed an empirical tight binding (TB) calculation which is able to reproduce the main experimental features. In order to limit the complexity of the calculation, the model considers a single orbital per atomic site with sp_z symmetry. While this is an approximation, we expect contributions from other orbital symmetries to be small in the energy range of interest. This is supported by recent results for the isostructural Bi-Ge(111) interface [24]. The primitive unit cell contains three Bi atoms, labelled a, b and c in Fig. 9. In the same figure the five inequivalent hopping terms are indicated by arrows. All the other terms can be generated by symmetry. The Si(111) substrate is only indirectly taken into account through the effective hopping parameters. A calculation of the transfer integrals is a non trivial computational task, which clearly goes beyond the scope of this work. Therefore we defined them in a purely phenomenological way, assuming an inverse power-law dependence of the distance d between two centers: $V(d) = ad^{-b}$. The prefactor a determines the bandwidths, while the exponent b determines details of the dispersion. There is obviously no angular dependence for sp_z states. The Bi-Bi distance within a single trimer was set to 2.6 Å, which is very close to literature values [22, 33]. In the actual calculation we included interactions up to 4th nearest neighbors. The required overall resemblance with the experimental dispersion significantly limits the acceptable parameter space. The chosen values are summarized in Table II of the Appendix.

Figure 10 illustrates the results of the TB model before the inclusion of a RB interaction. The calculation yields three bands, corresponding to the three orbitals per unit cell. The two higher lying states are shown for the $\bar{\Gamma}\bar{M}\bar{\Gamma}$ (a) and $\bar{\Gamma}\bar{K}\bar{M}$ (b) directions in Fig. 10. They can be associated to the experimental features of Fig. 4. The model correctly predicts a double degeneracy at the $\bar{\Gamma}$ and \bar{K} points, independent of the parameter values. A double degeneracy is imposed by the C_{3v} symmetry of these points for the trimer structure. The \bar{M} point has a lower symmetry (C_{1h}) and therefore no degeneracy is expected there. An interesting result is the presence of two maxima for S_1 on both sides of \bar{M} along $\bar{\Gamma}\bar{M}\bar{\Gamma}$. This hallmark of the trimer structure, which is not observed in simple hexagonal structures, has been reported for other similar systems [34, 35]. We shall see below that it plays an important role in the appearance of a *giant* SO splitting in Bi-Si(111).

We consider next the effect of the SO interaction, by adding a RB term to the TB hamiltonian [36–39]:

$$H_{TB} = \sum_{\langle i,j \rangle} V_{ij} c_{is}^\dagger c_{js} + i \sum_{\langle i,j \rangle > s, s'} \lambda_{ij} c_{is}^\dagger (\boldsymbol{\sigma} \times \hat{\mathbf{d}}_{ij})_z c_{js'} \quad (10)$$

The first term is the usual spin-independent TB hamiltonian, while the second term is the appropriate TB form for the Rashba interaction. c_{is}^\dagger (c_{is}) is the creation (annihilation) operator of an electron with spin s (\uparrow or \downarrow) on atomic site i , V_{ij} and λ_{ij} are the transfer integrals and the SO coefficients. The latter are generated by a similar power-law function of the distance, but with independent parameters (see Table II of the

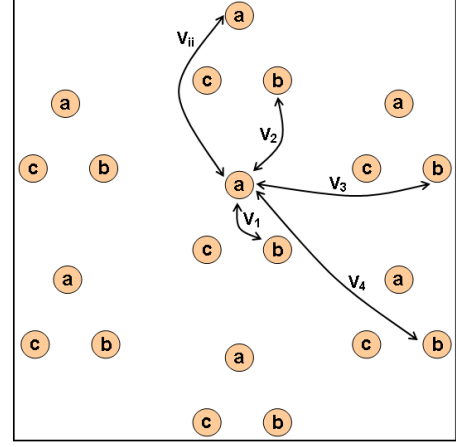


FIG. 9: (color online) Schematics of the cell used for the TB calculation, with the definition of the inequivalent transfer integrals.

Appendix). $\boldsymbol{\sigma}$ is the vector of the Pauli matrices and $\hat{\mathbf{d}}_{ij}$ is the vector connecting site j to site i .

The six basis vectors of a site-spin representation are, with obvious notation, $|a \uparrow\rangle$, $|b \uparrow\rangle$, $|c \uparrow\rangle$, $|a \downarrow\rangle$, $|b \downarrow\rangle$, $|c \downarrow\rangle$. In this representation, the hamiltonian matrix has the form:

$$H_{TB} = \begin{pmatrix} H_0 & H_R \\ H_R^* & H_0 \end{pmatrix}. \quad (11)$$

H_0 is the 3×3 spin-independent TB hamiltonian which describes states of equal spin. H_R is a 3×3 matrix generated by the second term of H_{TB} , which describes the coupling of electrons with opposite spins. Our method is essentially akin to the TB model of Ref. 11 and can qualitatively describe the SO split bands, namely their topology.

Figure 11 shows the band structure of the TB model with RB interaction, for the parameters which best reproduce the experimental results. The first obvious effect of the RB interaction is that all states are now split. Both S_1 and S_2 are doubly-degenerate at $\bar{\Gamma}$, and exhibit an isotropic dispersion around this point (Fig. 11 (a)). By moving out of the high-symmetry line (Fig. 11 (b)) the degeneracy is lifted, as expected for the usual RB scenario of Fig. 1. The spin-split branches cross again at \bar{M} , as required by time-reversal symmetry. Here, the dispersion of S_1 is strongly anisotropic. The splitting of S_1 along the $\bar{\Gamma}\bar{M}\bar{\Gamma}$ direction is much larger than that of S_2 . It is also much larger than the splitting of S_1 around $\bar{\Gamma}$. By contrast, it is small along the SBZ boundary $\bar{K}\bar{M}\bar{K}$ (Fig. 11 (c)). All these features of the band structure agree with the ARPES results, and also with the results of first-principles calculations [22, 23]. The calculated energy difference $E_R(\bar{M})$ between the band crossing at \bar{M} and the band maximum is nonetheless smaller than the experimental one.

A comparison of Fig. 10 (a) and Fig. 11 (a) shows that the large SO splitting of S_1 is a consequence of the split maxima on opposite sides of \bar{M} , rather than the result of a large SO coupling. In a way, the conditions for a large momentum splitting are already present in the band structure, and

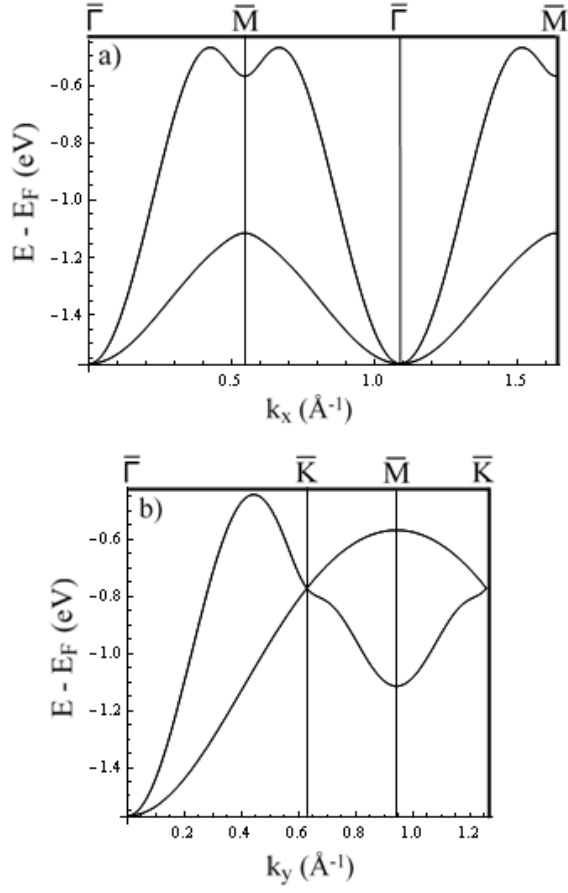


FIG. 10: Calculated band dispersion of the two higher lying states according to the TB model without RB interaction, along the $\bar{\Gamma}\bar{M}\bar{\Gamma}$ (a) and the $\bar{\Gamma}\bar{K}\bar{M}\bar{K}$ (b) high-symmetry directions.

the main effect of the SO interaction is to split in energy the two subbands. Indeed for S_2 , which has a maximum at \bar{M} in the parent structure, the Rashba splitting is small. The origin of the large momentum separation is therefore rather different from that of the ‘giant’ splitting observed at metallic interfaces like $\text{BiAg}_2/\text{Ag}(111)$ [14].

Figure 12 illustrates the energy evolution of the calculated CE contours near \bar{M} , across the spin-degeneracy point. The experimental contours are reproduced here for a qualitative comparison. A fully quantitative comparison is not possible due to the already mentioned difference in $E_R(\bar{M})$. The energies of the calculated contours were therefore adjusted to correspond to the experimental energies of the ARPES contours. The model yields open contours around \bar{M} , which are in good agreement with the topology of the experimental bands. The CE contours are shown on a broader momentum range in Fig. 13 (a) and (b) for two energies above, and in Fig. 13 (c) for an energy well below the crossing point. The shape of the contours is nearly circular near the bottom of the band at $\bar{\Gamma}$ (Fig. 13 (c)), and it evolves to a hexagonal and finally blossom-like shape at larger energy. The sixfold symmetry is the result of the threefold rotational symmetry and time-reversal symme-

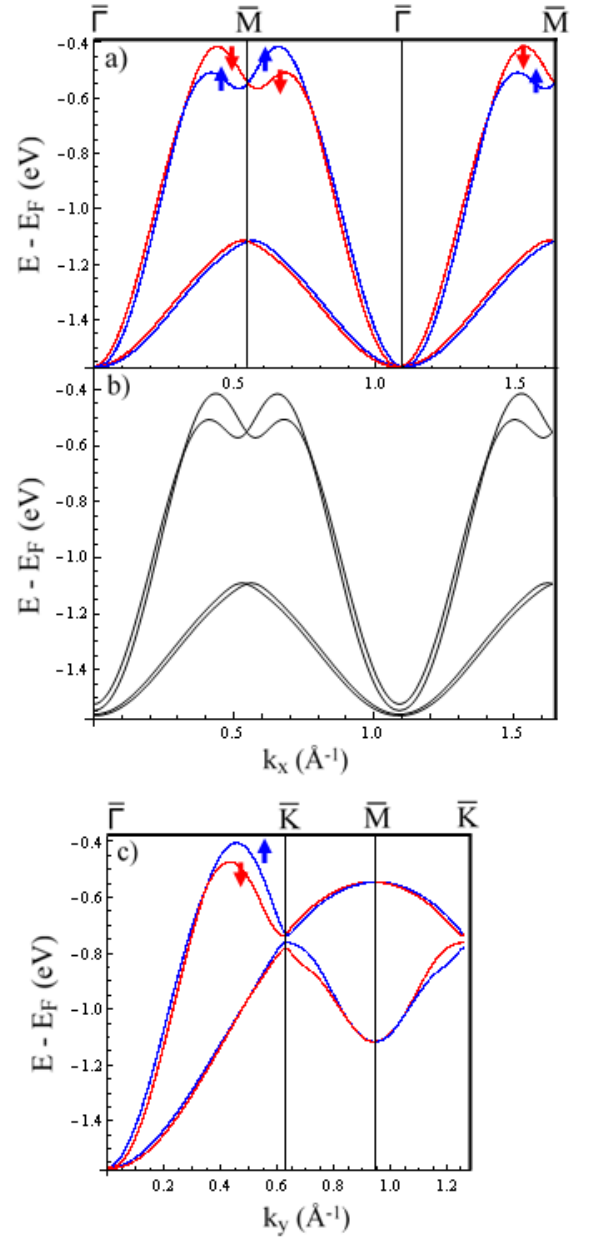


FIG. 11: (color online) Calculated bands for the TB model with SO (see Table II of the Appendix for the parameters) for: (a) the $\bar{\Gamma}\bar{M}\bar{\Gamma}$ direction; (b) the parallel cut b of Fig. 4 (d) ($k_y = 0.05 \text{\AA}^{-1}$); (c) the $\bar{\Gamma}\bar{K}\bar{M}\bar{K}$ direction. Arrows denote the main component of the spin polarization of the SO-split branches. The polarization difference is not 100% due to additional radial and out-of-plane components.

try. This is seen more clearly in Fig. 13 (d), where the SO parameters were artificially increased to enhance the splitting of the two subbands. Interestingly, the blossom-like shape of Fig. 13 (d) is identical to the one predicted by the anisotropic NFE model (see subsection C and Ref. [15]) but the tips now point along the $\bar{\Gamma}\bar{M}\bar{\Gamma}$ direction. Following the same reasoning as in the last paragraph of subsection C, the underlying orientation of the 3D spin polarization vector correctly defines

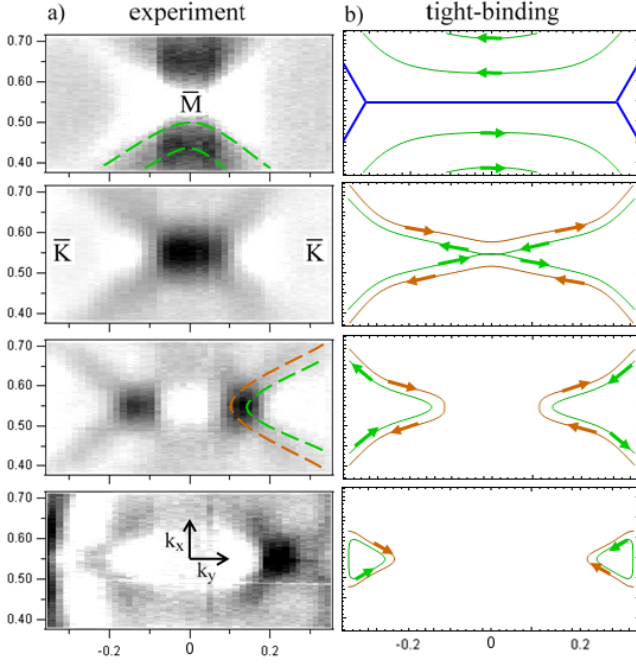


FIG. 12: (color online) (a) CE ARPES contours. The dashed curves on the experimental maps are guides to the eye. Green (light gray) and brown (dark gray) colors indicate positive and negative values of tangential spin polarization. (b) CE contours for the TB model. The arrows indicate the in-plane projection of the spin polarization. The energies were adjusted to correspond to the experimental values.

$\bar{\Gamma}\bar{K}\bar{M}$ as the only mirror plane of our system.

IV. CONCLUSIONS AND OUTLOOK

We performed a detailed ARPES study of the SO-split electronic states in the 1 ML trimer phase of the Bi-Si(111) interface. We paid special attention to the region of k -space close to the \bar{M} point, where the topmost S_1 hybrid surface state is both not degenerate with bulk states and distinct from other surface-related features. This region is of particular interest because there S_1 exhibits a large and non-conventional Rashba-like splitting. Energy-dependent constant energy contours clarify the complex topology of the SO-split states, and underline the differences with a standard RB scenario. The ARPES data show that the interface has an insulating character, but the Fermi level could be moved into the SO-split bands by applying an external electric potential in a back-gated structure. It should then be possible to advantageously exploit the large momentum separation of the two spin-polarized subbands in a spin field-effect transistor [17, 18].

We have used the predictions of three simple models for a 2DEG in the presence of SO interaction as guidelines for the interpretation of the experimental results. The comparison of the NFE and local-orbital schemes, which proceed from opposite starting points, has a certain didactic value. Moreover we were able to assess the limits of the various approaches

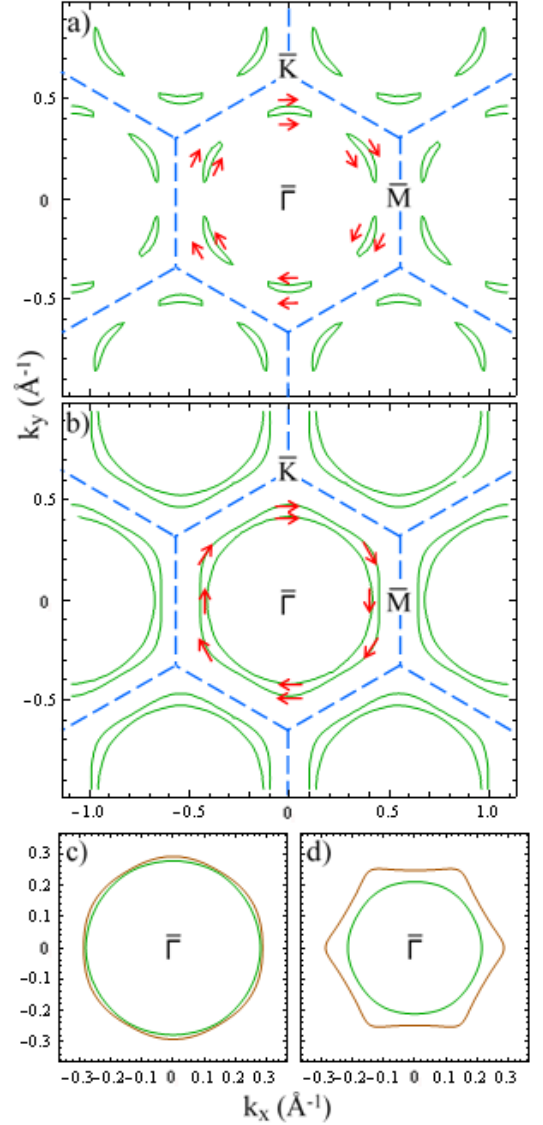


FIG. 13: (color online) CE contours of the TB model for energies above (a), (b) and well below (c) the spin degenerate point at \bar{M} . Arrows indicate the in-plane projection of the spin polarization. (d) is the same as (c) for an eightfold increase in the SO parameters. Green (light gray) and brown (dark gray) colors indicate positive and negative values of tangential spin polarization.

applied to the Bi-Si(111) case. The ARPES results and CE contours are well described by a NFE RB effect in a sufficiently small region around the $\bar{\Gamma}$ point. Further away from $\bar{\Gamma}$ the isotropic NFE model must be refined to include an in-plane asymmetry. Near the SZB, the specific symmetry properties of the interface determine the characteristics of the SO splitting [40], and only the empirical TB model captures the salient features of the electronic structure. The same model predicts a peculiar spin texture (Fig. 13 (a)). Hole pockets with a non-vortical spin arrangement are reminiscent of the teardrop Fermi surface contours of the topological insulator $\text{Bi}_{1-x}\text{Sb}_x$ [41]. Within a few meV the pockets develop into two

connected concentric contour with the same spin polarization (Fig. 13 (b)). This new prediction calls for an experimental verification by spin-resolved ARPES.

Our TB approximation obviously cannot reproduce all the details of the complicated electronic structure. More elaborate TB schemes could be implemented by extending the set of local orbitals to other symmetries, by treating in an explicit way the hybridization with the substrate, and by deriving the relevant transfer integrals from a direct calculation. However, the actual merit of such schemes would be dubious, since the computational complexity would approach that of first principles calculations, and since the immediate simplicity of the simple model would be lost. As a matter of fact, the proposed approach remains a helpful tool in the experimentalist's hands to interpret the complex band structure.

The main insight from our analysis of the new experimental data is the realization that the *giant* SO splitting at this interface is not primarily controlled by a large atomic SO parameter, as in the case of BiAg₂/Ag(111) and other metallic surface alloys [14]. On the contrary, the effect is largely due to a peculiar feature in the band structure, namely the presence of symmetrically split maxima around the \bar{M} point. This appears as a new, unexpected mechanism to achieve large spin separation at an interface. The underlying band feature is characteristic of the trimer structure, and it has been identified at other similar interfaces [34, 35]. We may therefore anticipate that similar large "Rashba"-like effects could be discovered in other systems characterized by moderate SO parameters.

It is a pleasure to acknowledge fruitful discussions with A. Baldereschi, J. Henk, I. Rousochatzakis and K. Sakamoto. We also thank L. Moreschini and L. Casanellas for help during the early stage of this work. E.F. acknowledges the Alexander S. Onassis Public Benefit Foundation for the award of a scholarship. This research was supported by the Swiss NSF and the NCCR MaNEP.

APPENDIX

The phenomenological parameters of the models are summarized in the following tables:

TABLE I: Parameters of the NFE modes. The potential value refers to the 1st Fourier coefficient of the crystal potential $V(r)$.

parameter	isotropic NFE	anisotropic NFE
m^* (m_e)	0.8	0.8
c (eV.Å ³)	0	4.8
α_R (eV.Å)	1.1	1.1
$ V_G $ (eV)	0.3	0.3

TABLE II: Parameters of the TB model. The hopping and SO parameters are generated by power law functions of the distance d (i.e. ad^{-b}).

	V_{ij}	λ_{ij}
prefactor a	-2.94	0.15 (1.20 in Fig. 13 (d))
exponent b	1.13	0.80

- [1] G. Dresselhaus, Phys. Rev. **100**, 580 (1955).
- [2] J. Könenmann, R. J. Haug, D. K. Maude, V. I. Fal'ko, and B. L. Altshuler, Phys. Rev. Lett. **94**, 226404 (2005).
- [3] Y. A. Bychkov and E. I. Rashba, JETP Lett. **39**, 78 (1984).
- [4] S. LaShell, B. McDougall, and E. Jensen, Phys. Rev. Lett. **77**, 3419 (1996).
- [5] E. Rotenberg, J. W. Chung, and S. D. Kevan, Phys. Rev. Lett. **82**, 4066 (1999).
- [6] M. Hochstrasser, J. G. Tobin, E. Rotenberg, and S. D. Kevan, Phys. Rev. Lett. **89**, 216802 (2002).
- [7] F. Reinert, J. Phys. Condens. Matter **15**, S693 (2003).
- [8] Y. M. Koroteev, G. Bihlmayer, J. E. Gayone, E. V. Chulkov, S. Blügel, P. M. Echenique, and P. Hofmann, Phys. Rev. Lett. **93**, 046403 (2004).
- [9] J. Henk, M. Hoesch, J. Osterwalder, A. Ernst, and P. Bruno, J. Phys. Condens. Matter **16**, 7581 (2004).
- [10] D. Malterre, B. Kierren, Y. Fagot-Revurat, S. Pons, A. Tejada, C. Didiot, H. Cercellier, and A. Bendounan, New. J. Phys. **9**, 391 (2007).
- [11] L. Petersen and P. Hedegard, Surf. Sci. **459**, 49 (2000).
- [12] G. Bihlmayer, Y. M. Koroteev, P. M. Echenique, E. V. Chulkov, and S. Blügel, Surf. Sci. **600**, 3888 (2006).
- [13] M. Nagano, A. Kodama, T. Shishidou, and T. Oguchi, J. Phys.: Condens. Matter **21**, 064239 (2009).
- [14] C. R. Ast, J. Henk, A. Ernst, L. Moreschini, M. C. Falub, D. Pacilé, P. Bruno, K. Kern, and M. Grioni, Phys. Rev. Lett. **98**, 186807 (2007).
- [15] J. Prempere, M. Trautmann, J. Henk, and P. Bruno, Phys. Rev. B **76**, 073310 (2007).
- [16] G. Bihlmayer, S. Blügel, and E. V. Chulkov, Phys. Rev. B **75**, 195414 (2007).
- [17] S. Datta and B. Das, Appl. Phys. Lett. **56**, 665 (1990).
- [18] H. C. Koo, J. H. Kwon, J. Eom, J. Chang, S. H. Han, and M. Johnson, Science **325**, 1515 (2009).
- [19] E. Frantzeskakis, S. Pons, H. Mirhosseini, J. Henk, C. R. Ast, and M. Grioni, Phys. Rev. Lett. **101**, 196805 (2008).
- [20] T. Hirahara, T. Nagao, I. Matsuda, G. Bihlmayer, E. V. Chulkov, Y. M. Koroteev, P. M. Echenique, M. Saito, and S. Hasegawa, Phys. Rev. Lett. **97**, 146803 (2006).
- [21] K. He, T. Hirahara, T. Okuda, S. Hasegawa, A. Kazizaki, and I. Matsuda, Phys. Rev. Lett. **101**, 107604 (2008).
- [22] I. Gierz, T. Suzuki, E. Frantzeskakis, S. Pons, S. Ostanin, A. Ernst, J. Henk, M. Grioni, K. Kern, and C. R. Ast, Phys. Rev. Lett. **103**, 046803 (2009).
- [23] K. Sakamoto, H. Kakuta, K. Sugawara, K. Miyamoto, A. Kimura, T. Kuzumaki, N. Ueno, E. Annese, J. Fujii, A. Kodama, et al., Phys. Rev. Lett. **103**, 156801 (2009).
- [24] S. Hatta, T. Aruga, Y. Ohtsubo, and H. Okuyama, Phys. Rev. B **80**, 113309 (2009).
- [25] K. Yaji, Y. Ohtsubo, S. Hatta, H. Okuyama, K. Miyamoto, T. Okuda, A. Kimura, H. Namatame, M. Taniguchi, and

- T. Aruga, *Nature Communications* **1**, 17 (2010).
- [26] S. Nakatani, T. Takahashi, Y. Kuwahara, and M. Aono, *Phys. Rev. B* **52**, R8711 (1995).
- [27] Y. K. Kim, J. S. Kim, C. C. Hwang, S. P. Shresta, and C. Y. Park, *Surf. Sci.* **498**, 116 (2002).
- [28] T. Kinoshita, S. Kono, and H. Nagayoshi, *J. of the Phys. Soc. of Japan* **56**, 2511 (1987).
- [29] Y. K. Kim, J. S. Kim, C. C. Hwang, S. P. Shresta, K. S. An, and C. Y. Park, *J. of the Korean Phys. Soc.* **39**, 1032 (2001).
- [30] C. Didiot, Y. Fagot-Revurat, S. Pons, B. Kierren, C. Chatelain, and D. Malterre, *Phys. Rev. B* **74**, 081404 (2006).
- [31] L. Moreschini, A. Bendounan, I. Gierz, C. R. Ast, H. Mirhosseini, H. Höchst, K. Kern, J. Henk, A. Ernst, S. Ostanin, et al., *Phys. Rev. B* **79**, 075424 (2009).
- [32] L. Fu, *Phys. Rev. Lett.* **103**, 266801 (2009).
- [33] K. J. Wan, T. Guo, W. K. Ford, and J. C. Hermanson, *Surf. Sci.* **261**, 69 (1992).
- [34] J. K. Kim, K. S. Kim, J. L. McChesney, E. Rotenberg, H. N. Hwang, C. C. Hwang, and H. W. Yeom, *Phys. Rev. B* **80**, 075312 (2009).
- [35] J. Y. Lee and M. H. Kang, *J. Korean Phys. Soc.* **53**, 3671 (2008).
- [36] C. L. Kane and E. J. Mele, *Phys. Rev. Lett.* **95**, 146802 (2005).
- [37] G. Liu, P. Zhang, Z. Wang, and S.-S. Li, *Phys. Rev. B* **79**, 035323 (2009).
- [38] G. Liu, Z. Wang, and S.-S. Li, *Physics Letters A* **373**, 2091 (2009).
- [39] A. Rüegg, J. Wen, and G. A. Fiete, *arXiv:0911.4722v1* (2009).
- [40] T. Oguchi and T. Shishidou, *J. Phys.: Condens. Matter* **21**, 092001 (2009).
- [41] D. Hsieh, Y. Xia, L. Wray, D. Qian, A. Pal, J. H. Dil, J. Osterwalder, F. Meier, G. Bihlmayer, C. L. Kane, et al., *Science* **323**, 919 (2009).